Journal of
Materials Chemistry C

Materials for optical, magnetic and electronic devices

ρ_{xy}

ρ_{xx}

ROYAL SOCIETY
OF **CHEMISTRY**

PAPER
Guowei Li *et al.*
Observation of the planar Hall effect in the
quasi-two-dimensional topological insulator
candidate $Ni_3Bi_2Se_2$

PAPER

Check for updates

Observation of the planar Hall effect in the quasi-two-dimensional topological insulator candidate Ni$_3$Bi$_2$Se$_2$†

Yuzhe Ma,[ab] Wen Sun,[ab] Qiunan Xu,[c] Xinming Wang,[bd] Aisha Aqeel[efg] and Guowei Li ◉ *[ab]

The observation of the planar Hall effect (PHE) sheds light on the spin textures and topological characteristics of materials, indicating potential applications in quantum computing and electronic devices. However, in bulk single crystals of topological insulators (TIs), where chiral anomaly is absent and the contribution of topological surface states can be overlooked, the origin of the PHE remains elusive. Here, we have obtained high-quality single crystals of Ni$_3$Bi$_2$Se$_2$ and systematically investigated their magneto-electric transport properties. The ordinary Hall resistivity reveals the simultaneous presence of electrons and holes. A π-period PHE, which depends on the relative angle with the driving electric and magnetic fields, has been observed, indicating the breaking of mirror reflection symmetry. The angular dependence of in-plane anisotropic magnetoresistance and the field-dependent PHE signal underscore the critical role of anisotropic orbital magnetoresistance. Our findings offer a platform for deepening our understanding of the PHE and its underlying mechanisms in TIs.

Introduction

In-plane anisotropic magnetoresistance (PAMR) and the planar Hall effect (PHE) refer to the variations in the in-plane longitudinal and transverse resistivity of a material, respectively, as a function of the angle between the in-plane current and the magnetic field. These phenomena have widespread application in tunneling magnetoresistive devices, magnetic sensors, and spintronic devices.[1–4] The remarkable advancements in the field of topological quantum matter over the last two decades

[a] CAS Key Laboratory of Magnetic Materials and Devices, Ningbo Institute of Materials Technology and Engineering, Chinese Academy of Sciences, Ningbo 315201, China. E-mail: liguowei@nimte.ac.cn

[b] University of Chinese Academy of Sciences, 19 A Yuquan Rd, Shijingshan District, Beijing 100049, China

[c] Qingdao Institute for Theoretical and Computational Sciences Shandong University, Qingdao 266237, China

[d] Public Technical Service Center, Ningbo Institute of Materials Technology and Engineering, Chinese Academy of Sciences, Ningbo 315201, China

[e] Physics Department, Technical University of Munich, Garching, Germany

[f] Munich Center for Quantum Science and Technology (MCQST), Munich, Germany

[g] Institute of Physics, University of Augsburg, Augsburg, Germany

have sparked significant interest in investigating these effects. In topological semimetals exhibiting a chiral anomaly, chiral charges are transferred between two Weyl nodes of opposite chirality when the electric and magnetic fields are coplanar. The PHE manifests with an increasing magnetic field and has also been considered as additional evidence for identifying the Weyl/Dirac nature of materials, alongside negative magnetoresistance (NMR).[5–11] To date, such phenomena have been documented in various topological semimetals, including ZrTe$_5$,[12] GdPtBi,[7] WTe$_2$,[10] VAl$_3$,[13] and so on.[14,15] Additionally, several other physical mechanisms have been proposed to explain the PHE, such as spin–orbit coupling, in-plane orbital magnetoresistance anisotropy, and anisotropic magnetic backscattering.

In contrast, topological insulators (TIs) do not inherently exhibit a chiral anomaly, presenting a significant opportunity to unravel the origin of the PHE. However, the observation of the PHE and its origin within these materials remain obscure. Taskin *et al.* suggested that the PHE in TIs could be due to the anisotropic scattering rate, which stems from the anisotropic polarization of magnetic impurities.[16] However, Zheng *et al.* proposed that the PHE mainly comes from anisotropic backscattering, which arises from the tilt of the Dirac cone with nonlinear momentum terms induced by an in-plane magnetic field.[17] Beyond this, a quasi-classical theory related to Boltzmann transport equations was proposed, which indicates that the PHE signal can be induced by the Berry curvature of the conduction band in three-dimensional (3D) TIs even without

chiral anomaly.[18] Recent research on $Bi_{1.1}Sb_{0.9}Te_2S$ has shown that the spin-momentum locking surface states of the TI are crucial for the PHE, which can be attributed to the differential backscattering forbiddance for Dirac fermions of varying spins under a planar magnetic field.[19] Given the theoretical propositions and their associated controversies, there is a pressing need to investigate new potential TI materials that exhibit the PHE.

Compounds with the chemical formula $M_3A_2B_2$ (where M = Ni, Co, Rh, Pd, and Pt; A = In, Tl, Sn, Pb, and Bi; B = S and Se) have garnered substantial interest for their complex topological nature and unique physical properties. Examples include the ferromagnetic Weyl semimetal $Co_3Sn_2S_2$, notable for its exceptionally large anomalous Hall conductivity, PHE, and NMR.[20–23] The kagome metals $Ni_3In_2S_2$ and $Pd_3Bi_2S_2$ are recognized for their infinite Dirac nodal lines, extraordinarily high mobility, and magnetoresistance (MR).[24–26] Given these precedents, the parkerite compound $Ni_3Bi_2Se_2$ has captured our interest because of the observation of superconductivity.[27] More recently, it has been predicted to exhibit a 3D topological insulator phase.[28,29] Moreover, first-principles calculations predict that $Ni_3Bi_2Se_2$ exhibits a three-dimensional strong TI phase with Z2 invariants (1;111) (Table S1, ESI†). This is distinct from the two-dimensional topological insulator with a corresponding Chern invariant.[30,31] This makes it a promising platform for investigating the PHE and other exotic physical phenomena, such as topological superconductivity.

In this study, we have successfully synthesized $Ni_3Bi_2Se_2$ single crystals using the Bi flux method and have comprehensively characterized their transport properties. The MR demonstrates notable anisotropy, reaching 12% for the magnetic field perpendicular ($B_\perp$) to the ab plane and approximately 1% for the magnetic field parallel ($B_\parallel$) to the ab plane, under a 9 T magnetic field at 2 K with the current flowing within the ab plane. Additionally, a distinct PHE signal with π periodicity was

observed when the external magnetic field was applied in a coplanar orientation with the current in the ab plane. Further analysis indicates that the PHE is primarily due to the anisotropy of the in-plane orbital magnetoresistance.

Experimental details

$Ni_3Bi_2Se_2$ single crystals were synthesized using a flux growth method, utilizing excess Bi as the flux. The starting materials consisted of Ni powder (99.99% purity), Bi shot (99.99% purity), and Se powder (99.99% purity), which were measured in a molar ratio of 1:3:1.2. These materials were placed into a fritted alumina crucible set (referred to as a Canfield Crucible Set)[32] and then sealed in a fused quartz tube under a partial argon pressure. The tube was subsequently heated to 1000 °C over 6 hours, maintained at this temperature for 20 hours, then cooled to 900 °C over 4 hours and held at this temperature for 10 hours. Following this, it was slowly cooled to 550 °C at a rate of 3 °C/hour. At this temperature, the remaining liquid was separated from the crystals through a centrifugation process.[33]

The crystal structure of the as-grown single crystals was determined using a Bruker D8 ADVANCE diffractometer (Cu Kα radiation, λ = 1.54178 Å) operating at a voltage of 40 kV and a current of 40 mA at 293 K. The single crystal X-ray diffraction (SXRD) data of $Ni_3Bi_2Se_2$ were collected using a Bruker D8 VENTURE single crystal diffractometer with multilayer monochromatized Mo Kα radiation (λ = 0.71073 Å) at 223 K, and the crystal structure was solved by direct methods and refined by the full-matrix least-squares method on F2 with the SHELXL software.[34,35] The composition characterization was carried out using a scanning electron microscope (SEM, ZEISS EVO18) equipped with an energy-dispersive X-ray spectroscopy (EDX) detector. For each of the two crystals from the same batch, 5 spots in different regions were measured, and the composition homogeneity of the crystal was determined by elemental mapping. The X-ray photoelectron spectroscopy (XPS) spectra were obtained using an X-ray photoelectron spectrometer (Axis Ultra DLD, Kratos). The resistivity, MR, and ordinary Hall effect measurements were performed using the standard six-probe technique in a physical property measurement system (PPMS, quantum design). The angle-dependent out-plane and in-plane transport measurements (i.e., angular magnetoresistance (AMR), PHE, and PAMR) were carried out using a PPMS by using a rotation option. The rotator inset was used to tilt the angle between the magnetic field and the current. To eliminate the effect of non-uniform thickness, samples for all measurements were cleaved from grown thicker crystals using a bistoury. The electronic band structures are theoretically studied using the Vienna Ab initio Simulation Package[36] based on density functional theory. The exchange–correlation potential was the generalized gradient approximation of the Perdew–Burke–Ernzerhof functional, and the cutoff energy was 400 eV. The k-mesh in the self-consistent process was 8 × 8 × 8.

Guowei Li is currently a principal investigator at the Ningbo Institute of Materials Technology & Engineering, Chinese Academy of Sciences, and the head of the Magnetic Materials for Energy Conversion group. He received his PhD degree from the University of Groningen in 2016 and subsequently served as a post-doctoral fellow and a group leader at the Max Planck Institute for Chemical Physics of Solids. His expertise and interests primarily focus on the growth of topological/magnetic single crystals, spin chemistry, and topological catalysis. In 2024, he was awarded a leadership position in the Max Planck Partner Group.

Guowei Li

This journal is © The Royal Society of Chemistry 2024

J. Mater. Chem. C, 2024, **12**, 13840–13846 | **13841**

Results and discussion

Millimeter-sized crystals with a silver-gray color were obtained, as illustrated in the inset of Fig. 1a. X-Ray diffraction (XRD) analysis indicates that $Ni_3Bi_2Se_2$ crystallizes in a parkerite-type structure, adopting the centrosymmetric monoclinic space group $C2/m$ (Fig. 1b). This structure is characterized by its pseudo-two-dimensional nature, forming a 3D framework through Ni–Bi ($d_{Ni–Bi}$ = 2.75–2.87 Å) and Ni–Se ($d_{Ni–Se}$ = 2.30–2.32 Å) bonds, which are stacked in the direction perpendicular to the ab plane. Within this structure, Ni atoms are coordinated by Se and Bi atoms, with Ni–Ni bonding creating one-dimensional chains along the a-axis. The X-ray diffraction pattern of the single crystal at room temperature is shown in Fig. 1a, with all peaks indexed by ($00l$) reflections, indicating the ab plane as the exposed surface. The lattice parameters, determined from SXRD data, are a = 11.1858(5) Å, b = 8.1601(5) Å, c = 8.0756(5) Å, and Z = 4, which align well with previous reports.[27] More detailed single crystal structure data are given in Tables S2–S5 (ESI†). The EDX spectrum suggests that the atomic ratio of Ni:Bi:Se (42.76%:28.72%:28.52%) in the as-grown $Ni_3Bi_2Se_2$ closely approximates the stoichiometric ratio (Fig. S1a, ESI†). Scanning electron microscopy images and elemental mapping reveal a uniform distribution of Ni, Bi, and Se within the crystal (Fig. S1b and Table S6, ESI†). Additionally, the XPS survey spectra (Fig. S2, ESI†) exhibit peaks at 853.5 eV (Ni 2p), 159.7 eV (Bi 4f), and 54.1 eV (Se 3d), demonstrating the presence of Ni, Bi, and Se in the $Ni_3Bi_2Se_2$ single crystal, which are consistent with the results of EDX and SXRD.

Angle-dependent out-of-plane (Fig. 1c) and in-plane (Fig. 1d) transport measurements were performed on a single crystal. Fig. 2a displays the temperature-dependent resistivity of the $Ni_3Bi_2Se_2$ single crystal in the absence of a magnetic field. The resistivity shows metallic-like behaviour with a residual-resistance ratio (RRR) (ρ_{300K}/ρ_{2K}) of approximately 5, comparable to that observed in other parkerite-type compounds.[37,38] This metallic-like behavior in topological insulators has been identified in several materials, such as $TaSe_3$, $CaBi_2$, and others, which is often attributed to the small energy gap.[39–42] Quantitatively, the resistivity in the temperature range of 20–300 K can be accurately described using the Bloch–Grüneisen (BG) model (eqn (1)), as depicted by the red solid line in Fig. 2a. This suggests that electron–phonon interaction is the primary scattering mechanism:

$$\rho(T) = \rho_0 + \left(\frac{T}{\theta_D}\right)^5 C \int_0^{\frac{\theta_D}{T}} \frac{z^5}{(e^z - 1)(1 - e^{-z})} dz \qquad (1)$$

where ρ_0, C, and θ_D are the residual resistivity at 2 K, electron–phonon interaction constant (a key parameter that controls the thermal relaxation rate between the electron and the lattice), and Debye temperature (the ratio of the energy corresponding to the highest vibration frequency of atoms in the crystal to the Boltzmann constant), respectively. The fitting parameters are ρ_0 = 31.25 μΩ cm, C = 258 μΩ cm, and θ_D = 180 K. The Debye temperature is close to the data fitted by specific heat.[27] We fit the resistivity curves at lower temperatures (2 K < T < 20 K) with the Fermi-liquid model using $\rho(T) = \rho_0 + AT^m$, as shown in the inset of Fig. 2(a), obtained m equals to 2.21, which deviate from the pure electron–electron (m = 2) and electron–phonon (m = 5) interaction.[43] The magnetic field dependence of MR, which is defined by $[\rho(B) - \rho(0)]/\rho(0) \times 100\%$, with the $B_\perp$ ab plane and the $I_\parallel$ ab plane at various temperatures, is depicted in Fig. 2b. MR that transitions from linear to parabolic without showing any signs of saturation, even at high magnetic fields and temperatures, is observed. This behavior differs from the weak anti-localization typically induced by topological surface states in TIs. Given that a similar phenomenon has also been observed in Bi-based semimetals,[44–46] the MR in the $Ni_3Bi_2Se_2$ crystal is inferred to originate from spin–orbit coupling interactions. In addition, the MR decreases with increasing temperature and reaches a minimum of ∼5% at 300 K under 9 T. Fig. 2c exhibits the angle-dependent MR curves by clockwise rotating the crystal in the zy plane under different magnetic fields. The MR decreases with increasing angles and reaches a minimum, which is 12% for $\theta = 0°$ and about 1% for $\theta = 90°$ at 2 K under 9 T, exhibiting a distinct anisotropy. No obvious NMR is detected in the case when the magnetic field is parallel to the current ($\theta = 90°$). The continuous anisotropic MR is further illustrated by a polar diagram, as displayed in Fig. 2d. The AMR shows a gourd shape, reflecting the geometry of the Fermi surfaces and their contribution to transport behavior. It can be explained by the pseudo-two-dimensional crystal structure of the $Ni_3Bi_2Se_2$ single crystal. The ordinary Hall effect of $Ni_3Bi_2Se_2$ at different temperatures is displayed in Fig. 2e. The Hall resistivity is found to be nonlinear and negatively correlated with the magnetic field, indicating that two types of carriers are present, and the electron-like carrier is dominant. According to the two-band model (see Fig. S3 in the ESI†), the carrier concentration and mobility at different temperatures obtained are shown in Fig. 2f, where n_h = 6.89×10^{21} cm^{-3}, n_e = 3.71×10^{21} cm^{-3}, μ_e = 379.02 cm^2 V^{-1} s^{-1}, and μ_h = 348.77 cm^2 V^{-1} s^{-1} at 2 K.

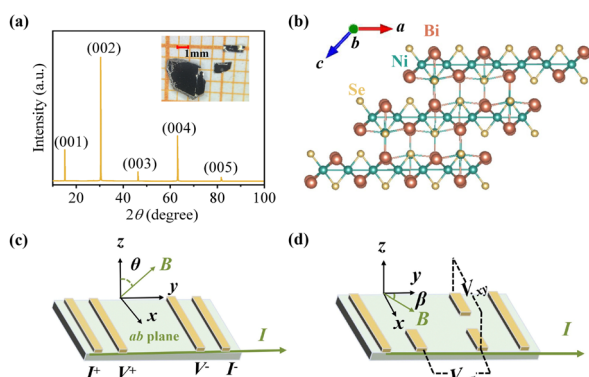**Fig. 1** (a) The X-ray diffraction pattern of the $Ni_3Bi_2Se_2$ crystal showing ($00l$) (l = integer) diffraction peaks, and the upper inset shows the optical image of the $Ni_3Bi_2Se_2$ single crystal. (b) The schematic crystal structure of $Ni_3Bi_2Se_2$. (c) The device configuration for out-of-plane transport measurement. (d) The schematic of the experimental configuration for the PHE and PAMR measurement.
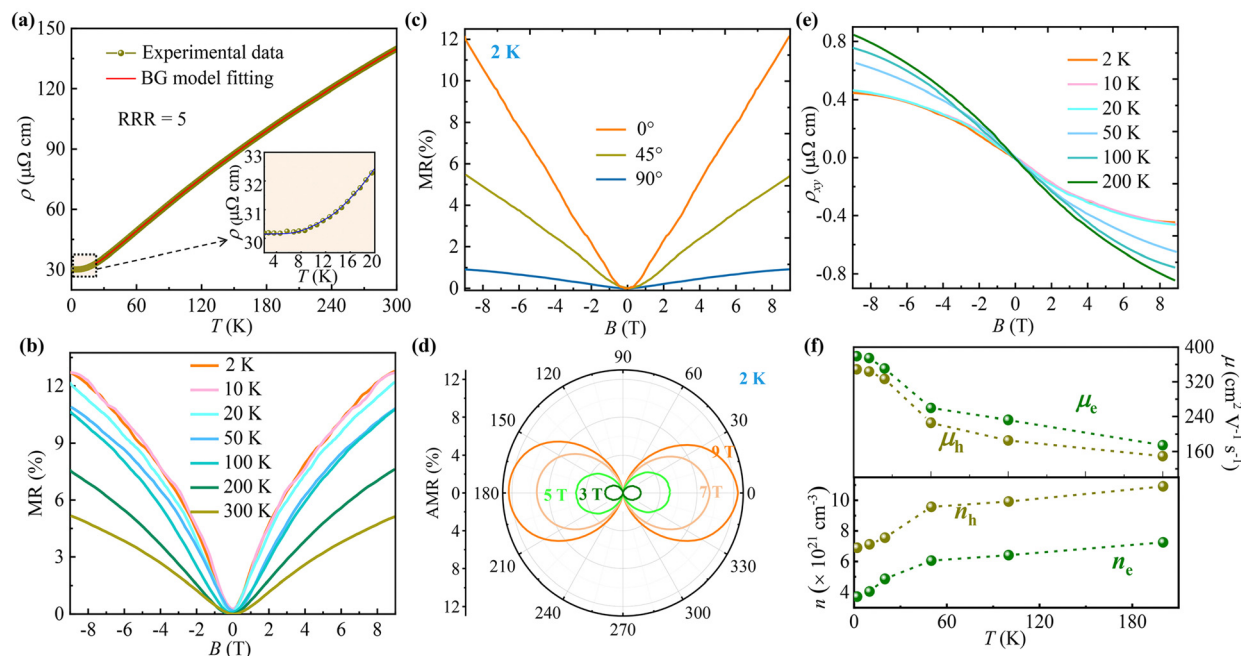
Fig. 2 (a) The temperature-dependent resistivity of the $Ni_3Bi_2Se_2$ single crystal measured with the $I_{\parallel}$ ab plane. The red solid line indicates the fitting by the BG model for $T \geq 20$ K. The inset shows the enlargement of low-temperature (2 K $< T <$ 20 K) resistivity and the corresponding fitting. (b) The MR as a function of the magnetic field at different temperatures with $I_{\parallel}$ ab for the $B_{\perp}$ ab plane. (c) The magnetic field-dependent MR of the $Ni_3Bi_2Se_2$ single crystal at different angles at 2 K. (d) The angle-dependent AMR at 2 K under different magnetic fields presented by a polar plot. (e) The magnetic field-dependent ordinary Hall resistivity at different temperatures. (f) The temperature-dependent carrier concentrations (n_h and n_e) and mobilities (μ_h and μ_e) were obtained from the two-band fitting.

To explore the in-plane transport properties, we systematically rotated the crystal clockwise in the xy plane under various magnetic fields to induce the PHE and PAMR, respectively. The magnetic field and current were aligned parallel to the single crystal's ab plane, with the angle between the magnetic field and the current defined as β. It is important to note that the observed PHE curves could be a composite of the planar Hall signal and the ordinary Hall signal, due to the potential out-of-plane component of the magnetic field. We assessed the planar Hall resistivity under both positive and negative fields and determined the average data. Moreover, misalignment in the transverse Hall-bar setup can lead to the appearance of both in-plane and out-of-plane longitudinal resistivity components.[13,47] Upon measuring several samples, we observed that the peaks and valleys of the PHE curves are positioned near 135°(315°) and 45°(225°), respectively, as shown in Fig. S4 (ESI†). This indicates that the contribution from the out-of-plane longitudinal resistivity component can be considered negligible. Furthermore, the in-plane longitudinal resistivity component can be ruled out using the formula $[\rho_{xy}(\beta) + \rho_{xy}(\pi - \beta)]/2$. In addition, the PHE and the PAMR phenomenon were repeatable for different samples, see Fig. S5 (ESI†).

The angle-dependent intrinsic PHE under various magnetic fields is presented in Fig. 3a. It was observed that the PHE curve distinctly displays π periodicity with respect to the angle β. This behavior can be interpreted under the theory of the PHE:[18,48]

$$\rho_{xy}^{\text{PHE}} = -\Delta\rho \sin\beta \cos\beta \qquad (2)$$

where $\Delta\rho = \rho_{\perp} - \rho_{\parallel}$ gives the resistivity anisotropy, $\rho_{\perp}$ and $\rho_{\parallel}$ are defined as the resistivity of $B \perp I$ ($\beta = 90°$) and $B \parallel I$ ($\beta = 0°$), respectively. Following this, we represented the PHE amplitude as a function of the magnetic field based on the fitting results, as illustrated in Fig. 3b. This relationship can be modeled (depicted by the blue solid line) using a power law. From these fittings, the power exponent is determined to be 1.29, which is lower than those observed in topological materials exhibiting chiral anomalies such as Te and $MoTe_2$.[17,49] It is well-established that for the PHE driven purely by the chiral anomaly, the amplitude of the PHE demonstrates quadratic behavior at higher magnetic fields, while it adheres to linear behavior at lower magnetic fields. This is contingent upon the comparative relationship between the magnetic field-induced length scale (L_a) and the chiral charge diffusion length (L_c).[50] However, the significant deviation of the power exponent from expected values suggests that the PHE signal in the $Ni_3Bi_2Se_2$ single crystal cannot be solely attributed to the chiral anomaly. It is important to note that the reciprocal of L_a signifies the coupling strength between trivial electric and chiral charges, which is further elucidated by the temperature dependence of the PHE amplitude. To delve deeper into the PHE behaviour, we analyzed the temperature-dependent PHE amplitude under 9 T, derived from the fitting data shown in Fig. 3c, and the findings are presented in Fig. 3d. Below 50 K, the PHE amplitude initially decreases sharply with temperature and then, above 50 K, it tapers off more gently up to 150 K. This trend suggests the persistence of PHE signals at elevated temperatures. The

This journal is © The Royal Society of Chemistry 2024

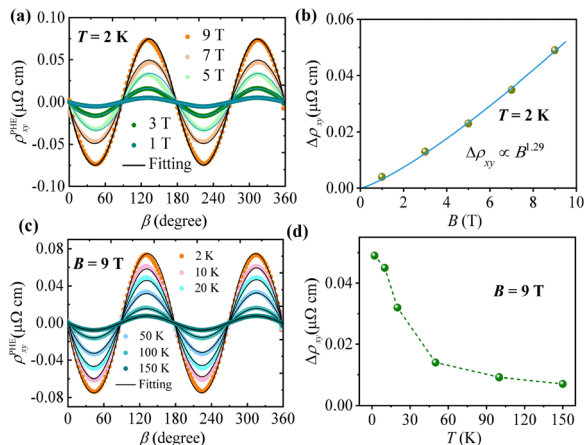*J. Mater. Chem. C*, 2024, **12**, 13840–13846 | **13843**

Fig. 3 (a) The angle-dependent planar Hall resistivity and the corresponding fitting curves under different magnetic fields at 2 K. (b) The magnetic-field-dependent amplitude of the PHE extracted by fitting the curves in (a) *via* theoretical equations. (c) The PHE data and the corresponding fitting curves at various temperatures under 9 T. (d) The temperature-dependent amplitude of the PHE extracted from the fitted curves in (c).
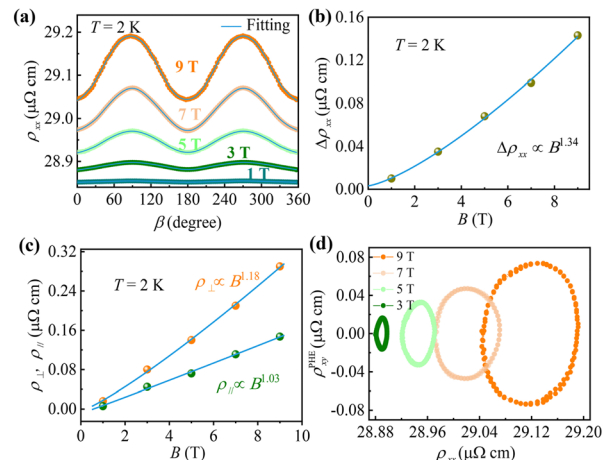

Fig. 4 (a) The angle dependence of planar resistivity under different magnetic fields at T = 2 K. (b) Magnetic field dependence of resistivity amplitude extracted from the fitting curves in (a), and the solid curve is the power law fitting result. (c) Magnetic field dependence of $\rho_\perp$ and $\rho_\parallel$ at 2 K. The blue line represents the power law fitting results. (d) Parametric plots of the planar Hall resistivity and planar resistivity showing the orbits at 2 K.

uniformly declining trend across the temperature range investigated implies the absence of electric and chiral charge coupling in the $Ni_3Bi_2Se_2$ single crystal. In addition, what we observed in Fig. 3d is different from that of topological semimetals with the chiral anomaly, such as Cd_3As_2.[17] In materials such as Cd_3As_2, within the low-temperature region, the amplitude of the PHE exhibits a minimal variation with increasing temperature. Conversely, in the high-temperature region, the PHE amplitude decreases significantly, a phenomenon typically ascribed to the thermal fluctuation effect.

Indeed, several mechanisms, apart from the chiral anomaly,[51] have been identified to contribute to the observed PHE, including anisotropic orbital magnetoresistance arising from Fermi pocket anisotropy, topological surface states characterized by spin-momentum locking,[18,52,53] and anisotropic magnetic scattering.[54] Given that $Ni_3Bi_2Se_2$ is a non-magnetic material, the possibility of magnetic scattering contributing to the PHE can be excluded. Furthermore, the higher carrier density (Fig. 2f) suggests that the surface states of this material are likely submerged within the bulk, implying a minimal or even a negligible influence of topological surface states on its transport properties. The small or negligible topological surface states can also be reflected in the electronic band structure of $Ni_3Bi_2Se_2$ (Fig. S6, ESI†). The bulk states with no global band gap and wide fluctuations will cover the surface state when projected the band structure onto the surface. At the same time, the DOS of the bulk state is far greater than the DOS of the surface state. Consequently, the origin of the PHE in this context requires further examination and clarification.

The angle-dependent in-plane resistivity under varying magnetic fields at 2 K is depicted in Fig. 4a. The in-plane resistivity adheres to a strict $\cos^2 \beta$ tendency with a period of π and can be accurately modeled using the equation provided (eqn (3)), as represented by the blue solid lines:

$$\rho_{xx} = \rho_\perp - \Delta\rho \cos^2 \beta \qquad (3)$$

It has been observed that the resistivity gradually increases with increasing magnetic fields when B is parallel to I ($\beta = 0°$ or 180°), a finding consistent with those presented in Fig. 2c and in contradiction to the NMR typically associated with the chiral anomaly. The obvious in-plane anisotropy in $Ni_3Bi_2Se_2$ may be ascribed to the anisotropic Fermi surface induced by in-plane anisotropy of the crystal structure, as depicted in Fig. S7 (ESI†). The amplitudes of in-plane resistivity, extracted from Fig. 4a, are plotted as a function of the magnetic field in Fig. 4b and can be well-fitted by the relationship $\Delta\rho_{xx} \propto B^{1.34}$. This is similar to the fitting results from the $\Delta\rho_{yx} - B$ curve (Fig. 3b), affirming the reliability of our measurements and analysis. Fig. 4c presents the parameters related to $\rho_\parallel$ and $\rho_\perp$ at 2 K, derived from the fitting results using eqn (3). For B parallel to I, $\rho_\parallel$ exhibits a slight increase with an intensifying magnetic field. Conversely, a noticeable enhancement in $\rho_\perp$ is observed when B is perpendicular to the I plane, indicating the potential presence of orbital magnetoresistance in the $Ni_3Bi_2Se_2$ single crystal, primarily originating from the anisotropy of transport parameters such as effective mass, scattering time, and mobility.[55]

For a deeper analysis of the potential physical mechanism underlying the PHE signal, we plotted the amplitude of the PHE against the in-plane resistivity of the $Ni_3Bi_2Se_2$ crystal under various magnetic fields and β as a parameter (Fig. 4d). The plots exhibit a "shock-wave" pattern and expand in the form of prolate ellipsoids towards larger resistivity values. Typically, in compounds where the pure chiral anomaly dominates, the orbit size increases more towards larger ρ_{xx} with an increasing magnetic field, due to the pumping of quasi-particles between Landau levels of opposite chirality. The parametric plot pattern usually displays concentric circles that expand uniformly with

13844 | *J. Mater. Chem. C*, 2024, **12**, 13840–13846

This journal is © The Royal Society of Chemistry 2024

increasing fields due to the equilibrium effect of quasi-particle scattering between the charge and chiral pockets, observed in materials like GdPtBi, Na_3Bi, *etc.*[7] In the case of the anisotropic orbital magnetoresistance mechanism, when the magnetic field is in-plane, the orbit starts with a small ρ_{xx} and gradually expands to a larger ρ_{xx} with increasing magnetic fields, forming a shock wave shape. Thus, the shock-wave pattern observed in our sample further supports the hypothesis that the PHE may be attributed to anisotropic orbital magnetoresistance.

To date, while the PHE curves seem to align well with equations associated with the chiral anomaly, all indications, such as the absence of negative magnetoresistance and the shock wave pattern, suggest that the chiral anomaly does not primarily account for the PHE signal. Instead, anisotropic orbital magnetoresistance appears to play a significant role in the PHE observed in the $Ni_3Bi_2Se_2$ single crystal. Additionally, Nandy *et al.* posited that the presence of surface-state transport in topological insulators is not a prerequisite for the occurrence of the PHE, which may instead be driven by the Berry curvature of the conduction band. To unequivocally ascertain the origin of the PHE signal, further studies are warranted. These should include the calculations of the electronic band structure, investigation of the morphology and anisotropy of the Fermi pockets in $Ni_3Bi_2Se_2$, and experiments focusing on the PHE phenomenon in thin films of varying thicknesses and orientations.

Conclusions

In this study, we provide a comprehensive analysis of the transport properties of the topological insulator candidate $Ni_3Bi_2Se_2$ single crystal. The ordinary Hall measurements highlight the simultaneous presence of both electrons and holes within the crystal. Furthermore, we observed a significant PHE and PAMR with a π period, occurring concurrently under coplanar electric and magnetic fields. The parametric plot reveals a shock-wave pattern, indicating that the observed PHE in $Ni_3Bi_2Se_2$ primarily arises from in-plane orbital magnetoresistance, as opposed to the chiral anomaly typically associated with NMR. Our results lay the groundwork for further theoretical exploration of the PHE in topological insulators, which is crucial not only for uncovering new physical mechanisms but also for the development of potential applications.

Author contributions

Yuzhe Ma: data curation, investigation, methodology, validation, and writing – original draft; Wen Sun: methodology and writing – review and editing; Qiunan Xu: methodology and formal analysis; Xinming Wang: methodology; Aisha Aqeel: methodology and writing – review and editing; Guowei Li: conceptualization, supervision, funding acquisition, and writing – review and editing.

Data availability

The data supporting this article have been included as part of the ESI.†

Conflicts of interest

There are no conflicts to declare.

Acknowledgements

References

1 H. X. Tang, R. K. Kawakami, D. D. Awschalom and M. L. Roukes, *Phys. Rev. Lett.*, 2003, **90**, 107201.

2 L. Fina, X. Marti, D. Yi, J. Liu, J. H. Chu, C. Rayan-Serrao, S. Suresha, A. B. Shick, J. Zelezny, T. Jungwirth, J. Fontcuberta and R. Ramesh, *Nat. Commun.*, 2014, **5**, 4671.

3 J. Zhou, W. Zhang, Y.-C. Lin, J. Cao, Y. Zhou, W. Jiang, H. Du, B. Tang, J. Shi, B. Jiang, X. Cao, B. Lin, Q. Fu, C. Zhu, W. Guo, Y. Huang, Y. Yao, S. S. P. Parkin, J. Zhou, Y. Gao, Y. Wang, Y. Hou, Y. Yao, K. Suenaga, X. Wu and Z. Liu, *Nature*, 2022, **611**, E1.

4 W. Ai, F. Chen, Z. Liu, X. Yuan, L. Zhang, Y. He, X. Dong, H. Fu, F. Luo, M. Deng, R. Wang and J. Wu, *Nat. Commun.*, 2024, **15**, 1259.

5 J. Xiong, S. K. Kushwaha, T. Liang, J. W. Krizan, M. Hirschberger, W. Wang, R. J. Cava and N. P. Ong, *Science*, 2015, **350**, 413–416.

6 X. Huang, L. Zhao, Y. Long, P. Wang, D. Chen, Z. Yang, H. Liang, M. Xue, H. Weng, Z. Fang, X. Dai and G. Chen, *Phys. Rev. X*, 2015, **5**, 031023.

7 S. Liang, J. Lin, S. Kushwaha, J. Xing, N. Ni, R. J. Cava and N. P. Ong, *Phys. Rev. X*, 2018, **8**, 031002.

8 S. Nandy, G. Sharma, A. Taraphder and S. Tewari, *Phys. Rev. Lett.*, 2017, **119**, 176804.

9 H. Li, H.-W. Wang, H. He, J. Wang and S.-Q. Shen, *Phys. Rev. B*, 2018, **97**, 201110.

10 P. Li, C. Zhang, Y. Wen, L. Cheng, G. Nichols, D. G. Cory, G.-X. Miao and X.-X. Zhang, *Phys. Rev. B*, 2019, **100**, 205128.

11 Q. Liu, F. Fei, B. Chen, X. Bo, B. Wei, S. Zhang, M. Zhang, F. Xie, M. Naveed, X. Wan, F. Song and B. Wang, *Phys. Rev. B*, 2019, **99**, 155119.

12 P. Li, C. H. Zhang, J. W. Zhang, Y. Wen and X. X. Zhang, *Phys. Rev. B*, 2018, **98**, 121108.

13 R. Singha, S. Roy, A. Pariari, B. Satpati and P. Mandal, *Phys. Rev. B*, 2018, **98**, 035110.

14 L. M. Schoop, M. N. Ali, C. Strasser, A. Topp, A. Varykhalov, D. Marchenko, V. Duppel, S. S. Parkin, B. V. Lotsch and C. R. Ast, *Nat. Commun.*, 2016, **7**, 11696.

This journal is © The Royal Society of Chemistry 2024

J. Mater. Chem. C, 2024, **12**, 13840–13846 | **13845**

15 L. M. Schoop, F. Pielnhofer and B. V. Lotsch, *Chem. Mater.*, 2018, **30**, 3155–3176.

16 A. A. Taskin, H. F. Legg, F. Yang, S. Sasaki, Y. Kanai, K. Matsumoto, A. Rosch and Y. Ando, *Nat. Commun.*, 2017, **8**, 1340.

17 S.-H. Zheng, H.-J. Duan, J.-K. Wang, J.-Y. Li, M.-X. Deng and R.-Q. Wang, *Phys. Rev. B*, 2020, **101**, 041408.

18 S. Nandy, A. Taraphder and S. Tewari, *Sci. Rep.*, 2018, **8**, 14983.

19 B. Wu, X.-C. Pan, W. Wu, F. Fei, B. Chen, Q. Liu, H. Bu, L. Cao, F. Song and B. Wang, *Appl. Phys. Lett.*, 2018, **113**, 011902.

20 D. F. Liu, A. J. Liang, E. K. Liu, Q. N. Xu, Y. W. Li, C. Chen, D. Pei, W. J. Shi, S. K. Mo, P. Dudin, T. Kim, C. Cacho, G. Li, Y. Sun, L. X. Yang, Z. K. Liu, S. S. P. Parkin, C. Felser and Y. L. Chen, *Science*, 2019, **365**, 1282.

21 E. Liu, Y. Sun, N. Kumar, L. Muechler, A. Sun, L. Jiao, S.-Y. Yang, D. Liu, A. Liang, Q. Xu, J. Kroder, V. Suess, H. Borrmann, C. Shekhar, Z. Wang, C. Xi, W. Wang, W. Schnelle, S. Wirth, Y. Chen, S. T. B. Goennenwein and C. Felser, *Nat. Phys.*, 2018, **14**, 1125.

22 Shama, R. K. Gopal and Y. Singh, *J. Magn. Magn. Mater.*, 2020, **502**, 166547.

23 S.-Y. Yang, J. Noky, J. Gayles, F. K. Dejene, Y. Sun, M. Dorr, Y. Skourski, C. Felser, M. N. Ali, E. Liu and S. S. P. Parkin, *Nano Lett.*, 2020, **20**, 7860–7867.

24 T. Zhang, T. Yilmaz, E. Vescovo, H. X. Li, R. G. Moore, H. N. Lee, H. Miao, S. Murakami and M. A. McGuire, *npj Comput. Mater.*, 2022, **8**, 2201.

25 H. Fang, M. Lyu, H. Su, J. Yuan, Y. Li, L. Xu, S. Liu, L. Wei, X. Liu, H. Yang, Q. Yao, M. Wang, Y. Guo, W. Shi, Y. Chen, E. Liu and Z. Liu, *Sci. China Mater.*, 2023, **66**, 2032–2038.

26 Shama, R. K. Gopal, G. Sheet and Y. Singh, *Sci. Rep.*, 2021, **11**, 12618.

27 T. Sakamoto, M. Wakeshima and Y. Hinatsu, *J. Condens. Matter Phys.*, 2006, **18**, 4417–4426.

28 M. G. Vergniory, L. Elcoro, C. Felser, N. Regnault, B. A. Bernevig and Z. Wang, *Nature*, 2019, **566**, 480–485.

29 T. Zhang, Y. Jiang, Z. Song, H. Huang, Y. He, Z. Fang, H. Weng and C. Fang, *Nature*, 2019, **566**, 475–479.

30 D. Xiao, M.-C. Chang and Q. Niu, *Rev. Mod. Phys.*, 2010, **82**, 1959.

31 S. Wang, P. Zhang, C. Ren, H. Tian, J. Pang, C. Song and M. Sun, *J. Supercond. Novel Magn.*, 2019, **32**, 2947–2957.

32 P. C. Canfield, T. Kong, U. S. Kaluarachchi and N. H. Jo, *Philos. Mag.*, 2016, **96**, 84–92.

33 P. C. Canfield, *Rep. Prog. Phys.*, 2020, **83**, 016501.

34 X.-L. Chen, J.-K. Liang and C. Wang, *Acta Phys. Sin.*, 1995, **4**, 259.

35 G. M. Sheldrick, *Acta Crystallogr., Sect. C: Struct. Chem.*, 2015, **71**(1), 3–8.

36 G. Kresse and J. Furthmüller, *Phys. Rev. B: Condens. Matter Mater. Phys.*, 1996, **54**, 11169.

37 T. Sakamoto, M. Wakeshima, Y. Hinatsu and K. Matsuhira, *Phys. Rev. B: Condens. Matter Mater. Phys.*, 2007, **75**, 060503.

38 Z. Y. Zhang, M. Ikeda, M. Utsumi, Y. Yamamoto, H. Goto, R. Eguchi, Y. F. Liao, H. Ishii, Y. Takabayashi, K. Hayashi, R. Kondo, T. C. Kobayashi and Y. Kubozono, *Inorg. Chem.*, 2024, **63**, 2553–2561.

39 S. Nie, L. Xing, R. Jin, W. Xie, Z. Wang and F. B. Prinz, *Phys. Rev. B*, 2018, **98**, 125143.

40 W. Xia, X. Shi, Y. Zhang, H. Su, Q. Wang, L. Ding, L. Chen, X. Wang, Z. Zou, N. Yu, L. Pi, Y. Hao, B. Li, Z. Zhu, W. Zhao, X. Kou and Y. Guo, *Phys. Rev. B*, 2020, **101**, 155117.

41 Q. Jiang, D. Wang, Z. Liu, Z. Jiang, H. Qian, X. Shen, A. Li, D. Shen, S. Qiao and M. Ye, *Phys. Rev. B*, 2021, **104**, 245112.

42 Y. Ma, Y. Wang and G. Wang, *Phys. Scr.*, 2023, **98**, 015002.

43 J. M. Ziman, *Electrons and Phonons: The Theory of Transport Phenomena in Solids*, Oxford University Press, 2001.

44 Y. Ma, Y. Wang and G. Wang, *EPL*, 2022, **138**, 36003.

45 S. Sasmal, R. Mondal, R. Kulkarni, A. Thamizhavel and B. Singh, *J. Condens. Matter Phys.*, 2020, **32**, 335701.

46 Z. Hou, Y. Wang, E. Liu, H. Zhang, W. Wang and G. Wu, *Appl. Phys. Lett.*, 2015, **107**, 202103.

47 H. Li, H.-W. Wang, H. He, J. Wang and S.-Q. Shen, *Phys. Rev. B*, 2018, **97**, 201110(R).

48 M. Wu, D. Tu, Y. Nie, S. Miao, W. Gao, Y. Han, X. Zhu, J. Zhou, W. Ning and M. Tian, *Nano Lett.*, 2022, **22**, 73–80.

49 N. Zhang, G. Zhao, L. Li, P. Wang, L. Xie, B. Cheng, H. Li, Z. Lin, C. Xi, J. Ke, M. Yang, J. He, Z. Sun, Z. Wang, Z. Zhang and C. Zeng, *Proc. Natl. Acad. Sci. U. S. A.*, 2020, **117**, 11337–11343.

50 A. A. Burkov, *Phys. Rev. B*, 2017, **96**, 041110(R).

51 S. Liang, J. Lin, S. Kushwaha, J. Xing, N. Ni, R. J. Cava and N. P. Ong, *Phys. Rev. X*, 2018, **8**, 031002.

52 A. Sulaev, M. Zeng, S.-Q. Shen, S. K. Cho, W. G. Zhu, Y. P. Feng, S. V. Eremeev, Y. Kawazoe, L. Shen and L. Wang, *Nano Lett.*, 2015, **15**(3), 2061–2066.

53 W. Rao, Y.-L. Zhou, Y.-J. Wu, H.-J. Duan, M.-X. Deng and R.-Q. Wang, *Phys. Rev. B*, 2021, **103**, 155415.

54 H. X. Tang, R. K. Kawakami, D. D. Awschalom and M. L. Roukes, *Phys. Rev. Lett.*, 2003, **90**, 107201.

55 S. Roy, R. Singha, A. Ghosh and P. Mandal, *Phys. Rev. Mater.*, 2021, **5**, 064203.

13846 | *J. Mater. Chem. C*, 2024, **12**, 13840–13846

This journal is © The Royal Society of Chemistry 2024